DUST STORM OF MY28 EFFECTS ON WATER VAPOR IN THE SOUTH POLAR REGION

C. W.S. Leung, *Jet Propulsion Laboratory/Caltech, Pasadena, USA (cecilia.leung@jpl.nasa.gov)*, **A. Pankine**, *Space Science Institute, Boulder, USA (apankine@SpaceScience.org)*, **L.Tamppari**, *Jet Propulsion Laboratory/Caltech, Pasadena, USA*, **M. Giuranna**, *Istituto Nazionale di Astrofisica, Veneto, Italy*, **A. Trokhimovskiy**, *Space Research Institute of the Russian Academy of Sciences (IKI RAS), Moscow, Russia*

Introduction:

Understanding the current water cycling in and out of the polar regions is key to unraveling the climatic history of Mars. Atmospheric circulation provides the main mechanism for the transport of around one-third of the mass of water in and out of the polar caps and in the annual exchange between the northern hemisphere to the southern hemisphere and back through the cross-equatorial Hadley circulation [1, 2]. Meanwhile up to ~ 10^{10}-10^{11} kg of water is deposited every year at the surface near the south pole due to the permanent cold trap for water vapor maintained by the presence of a residual CO_2 ice layer near the south pole [3,4]. Placing limits on the modern-day transport of water into the poles, and the water deposition rate in the south polar region (SPR) will allow us to better comprehend its important role in the mass balance and the modern-day stability of the polar ice cap.

A number of recent studies [5, 6, 7, 8, etc.] have highlighted the strong coupling between the water and dust cycles particularly during global dust storms (GDS), as the radiative effects of dust can dramatically alter atmospheric and surface temperatures, leading to significant modifications in the global circulation, water vertical distribution, water-ice cloud saturation conditions, as well as the rate of water escape.

The goal of this project is to test the hypothesis that Martian Global Dust Storms (GDS) can significantly affect the water cycle in the lower atmosphere. As part of the test we compare the evolution of the water vapor in the Southern Region of Interest (SRI) during the second half of MY28 and MY29. For the purposes of this project, we define the SRI to extend over 90°–40°S. For this work, we make use of datasets from the SPICAM IR and PFS/LW instruments aboard the Mars Express (ME) spacecraft, which conducted near simultaneous observations of the Martian atmosphere [9, 10].

Water cycle in the Southern Region of Interest:

Figure 1 illustrates the water cycle in the SRI during the second half of a typical year without a GDS. Figure 1 shows the evolution of SPICAM IR water vapor abundances (scaled by surface pressure to avoid topographic effects) in the latitudinal band 90°–80°S as a function of L_s. SPICAM IR observations [9] were obtained at local times of 10:00–15:00h for L_s=180°–250°, and 01:00–10:00h & 15:00–24:00h for L_s=250°–360°. Vapor abundances generally increase during southern spring and early summer (L_s=180°–280°) reflecting southward transport of vapor by atmospheric circulation and sublimation of seasonal surface frost. A temporary decrease in abundances at L_s=240°–255° coincides with a regional dust storm [11]. Vapor abundances reach their maximum values (~30 pr-μm) in this band at L_s~280°–295° after the seasonal polar cap completely disappears. Abundances start to decline after L_s~295°.

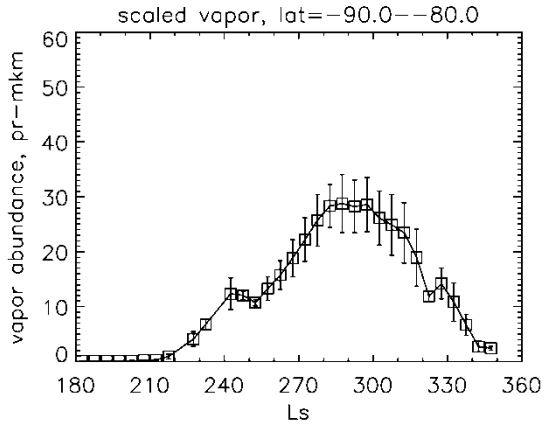

Figure 1. SPICAM IR zonally averaged scaled water vapor abundances in latitudinal band 90°–80°S for MY29 L_s=180–360°. Error bars indicate scatter of data within the band.

Figure 2 shows a polar map of SPICAM IR scaled water vapor abundances in MY29 L_s=280-290°, at the time when highest annual abundances were observed at the South Pole. This map shows that vapor abundances generally increase towards the pole.

Similar behavior of the water vapor in the SRI is observed in the PFS/LW data [10]. Local times of PFS/LW observations are similar to SPICAM IR times. Figure 3 shows the evolution of the zonally averaged PFS/LW water vapor abundances retrieved from data collected at approximately the same times and locations as the SPICAM IR data. Small systematic differences between the two datasets can be attributed to the differences between the two retrieval approaches and is generally within the uncertainty of the retrieval (~20%).

Spatial distribution of PFS/LW water vapor in

the SRI during MY29 L_s=280-290° shown in Figure 4 is generally similar to the SPICAM IR distribution (

Figure 2), except for more frequent appearances of high vapor abundances near the South Pole.

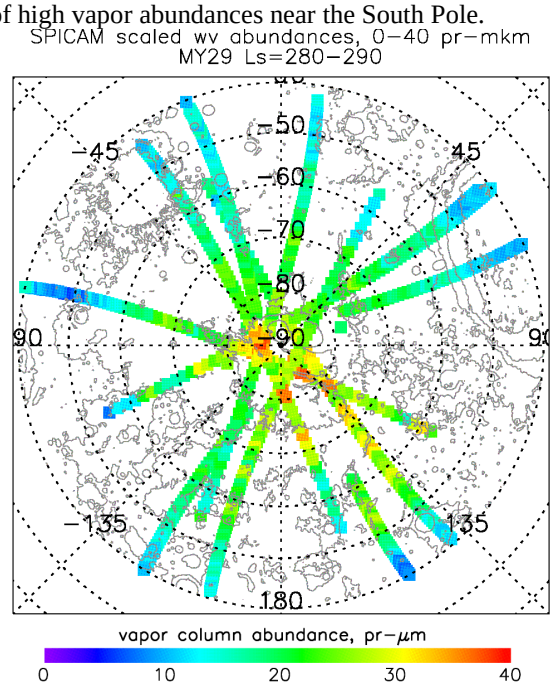

Figure 2. Polar map of SPICAM IR scaled water vapor abundances in MY29 L_s=280–290°. Thin contours are MOLA topography.

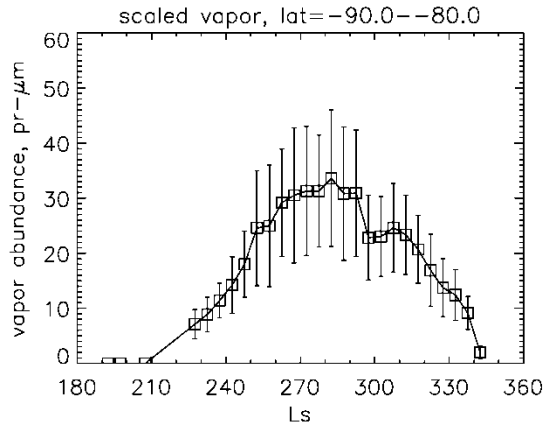

Figure 3. PFS/LW zonally averaged scaled water vapor abundances in latitudinal band 90°–80°S for MY29 L_s=180–360°.

Global Dust Storm of MY28:

A rare Martian GDS occurred in MY28 [12]. Figure 5 illustrates the evolution of the dust optical depth during the MY28 GDS in the latitudinal band 60°–50°S. The dust optical depth is from SPICAM IR dataset, and represents THEMIS dust observations [13] scaled to the wavelength of 1.4 μm [9] and by surface pressure, to remove the effects of topography.

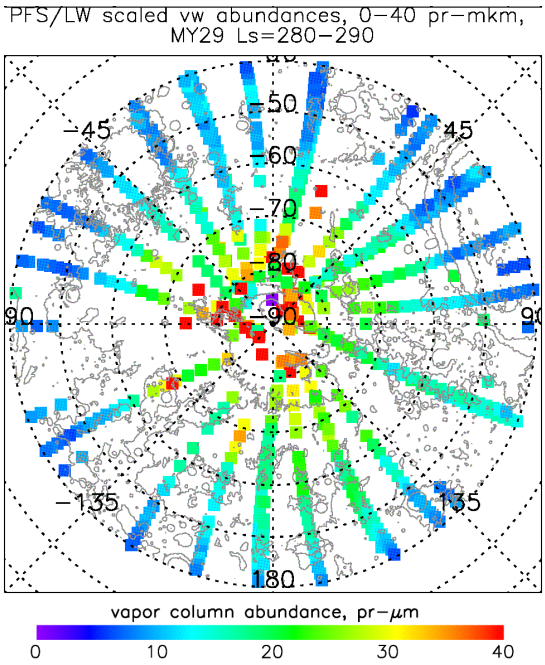

Figure 4. Polar map of PFS/LW scaled water vapor abundances in MY29 L_s=280–290°. Thin contours are MOLA topography.

The GDS started around L_s~260° and the dust optical depth did not return to pre-storm levels in this band until L_s~310°. At the peak of the storm (L_s~270–290°) average dust opacities in this band were close to 2. In contrast, the southward transport of dust into the SRI was limited, as illustrated in Figure 6, which shows dust opacity in the latitudinal band 90°–80°S. Here dust opacities increase to a value slightly higher than 1 at the peak of the storm (L_s~270°), and quickly return to pre-storm levels (by L_s=280°–290°).

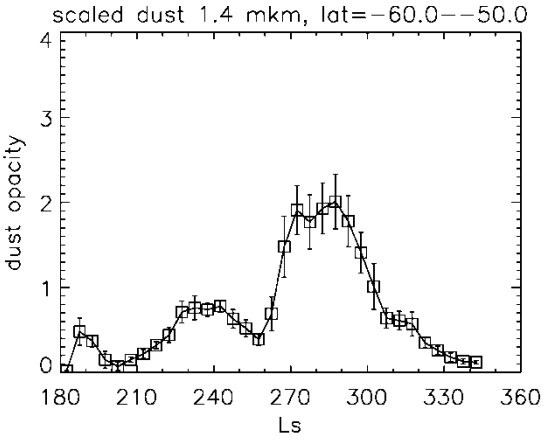

Figure 5. SPICAM IR zonally averaged scaled dust optical depth at 1.4 μm in latitudinal band 60°–50°S for MY28 L_s=180–360°.

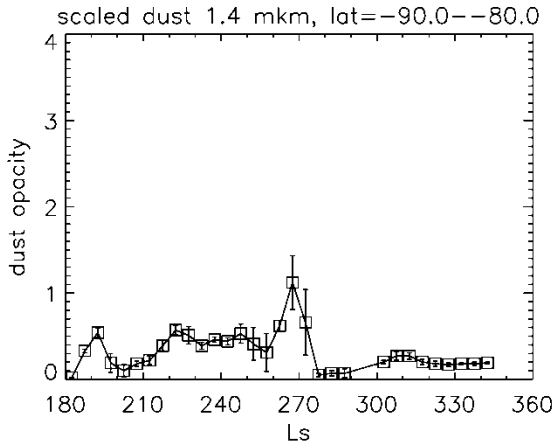

Figure 6. SPICAM IR zonally averaged scaled dust optical depth at 1.4 μm in latitudinal band 90°–80°S for MY28 L_s=180–360°.

Figure 7 shows evolution of the SPICAM IR water vapor abundances in the latitudinal band 90°–80°S before, during and after the GDS of MY28. During most of the spring the abundances increase quantitatively similar to the way they increased in MY29. The onset of the GDS at L_s~260° is marked by the sharp decrease in water vapor abundances that continues until L_s~290°. After that time abundances remain approximately constant until L_s~320° and begin decline afterwards. Abundances remain lower than in MY29 even after dust opacities return to pre-storm levels after L_s~280°–290°. Scaled dust distribution in SRI during that time is shown in Figure 8. Areas south of latitude ~75°S are clear of dust. Water vapor abundances over these areas (Figure 9) are noticeably lower than during the same time in MY29 (

Figure 2).

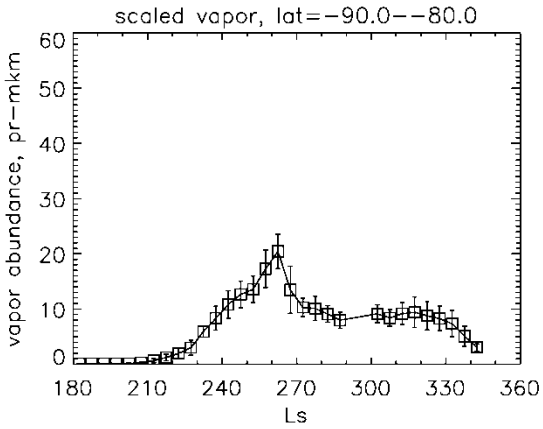

Figure 7. SPICAM IR zonally averaged scaled water vapor abundances in latitudinal band 90°–80°S for MY28 L_s=180–360°.

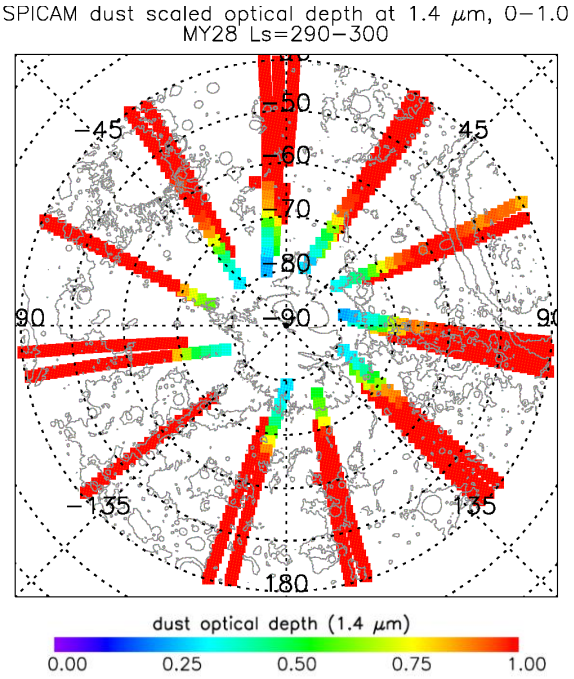

Figure 8. Polar map of SPICAM IR scaled dust optical depth at 1.4 μm in MY29 L_s=290–300°.

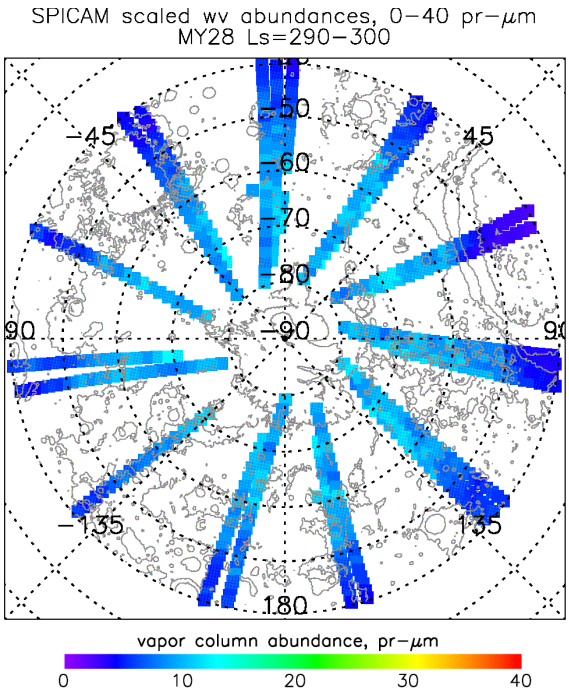

Figure 9. Polar map of SPICAM IR scaled water vapor abundances in MY28 L_s=290–300°.

PFS/LW abundances behave qualitatively similar to SPICAM IR in MY28 (Figure 10). PFS/LW abundances increase during summer, similar to the way they do in MY29. During this time PFS/LW abundances are higher than the SPICAM IR abundances at the same time, but there are fewer PFS/LW observations and the scatter of the retrieved vapor abundances in the band is relatively large. The onset of

the GDS at L_s~260° is marked by a decline in abundances that generally continues until the end of the summer (L_s~360°). The difference between vapor abundances between MY28 and MY29 is much smaller in PFS/LW retrievals than in SPICAM IR retrievals. The comparison between different PFS/LW years is difficult because there are significantly fewer PFS/LW retrievals in MY28. Figure 11 shows a polar map of the PFS/LW water vapor abundances in the SRI in MY28 L_s=290–300°. Abundances near the South Pole, where dust opacities are low, are similar to the PFS/LW abundances in MY29 at this time and are higher than the SPICAM IR abundances at the same time in MY28.

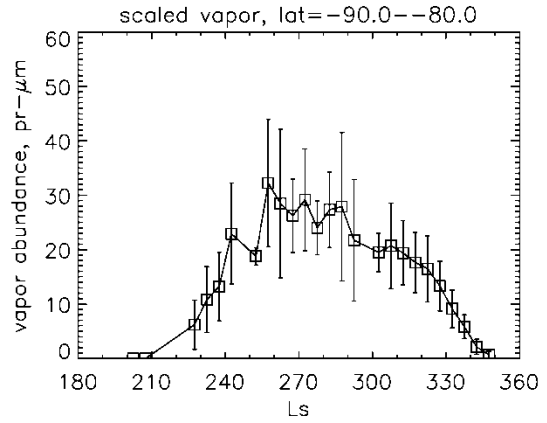

Figure 10. PFS/LW zonally averaged scaled water vapor abundances in latitudinal band 90°–80°S for MY28 L_s=180–360°.

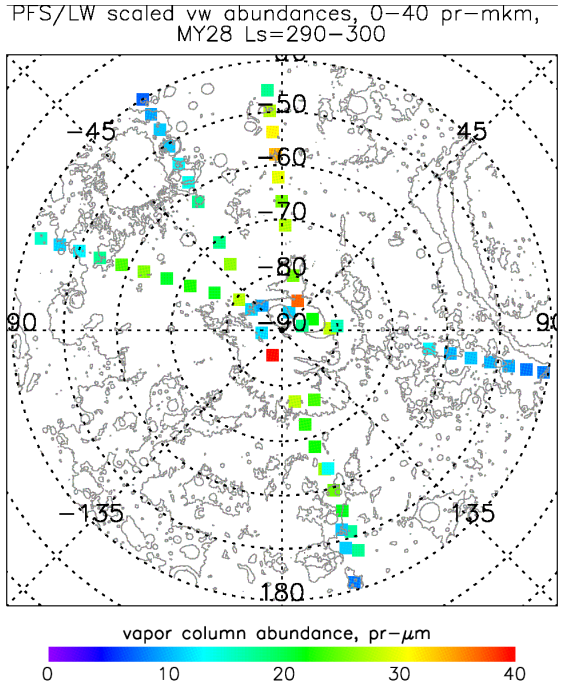

Figure 11. Polar map of PFS/LW scaled water vapor abundances in MY28 L_s=290–300°.

Conclusion: Water vapor abundances retrieved by SPICAM IR and PFS/LW in MY28 and MY29 show qualitatively similar behavior in the SRI in MY28 and MY29. Both datasets reflect a strong response of the water vapor cycle to the GDS of MY28. SPICAM IR abundances decline sharply at the onset of the GDS and remain lower than in the year without a GDS (e.g. MY29) even when the dust opacity decreases to pre-storm levels. This behavior may reflect the disruption of the southward transport of water vapor by atmospheric circulation by the GDS. PFS/LW abundances in MY28 also decline at the onset of the storm, but low number of retrievals and the large scatter in the values of retrieved abundances make comparison to MY29 difficult.

References:

[1] Houben et al.,1997. JGR, 102, 9069-9083. [2] Montmessin et al., 2004. JGR, 109, E10004, doi:10.1029/2004JE002284. [3] Jakosky, 1983a. Icarus, 55, 1 – 18, 1983a. [4] Richardson and Wilson, 2002a; JGR, 107, NO. E5, 10.1029/2001JE001536. [5] Vandaele et al., 2019. Nature, 568(7753), 521-525. [6] Fedorova et al., 2020. *Science*, *367*(6475), 297–300. [7] Chaffin et al., 2017. *Nature Geoscience*, *10*(3), 174–178. [8] Heavens et al., 2018. *Nature Astronomy*, *2*(2), 126–132. [9] Trokhimovskiy et al., 2015. Icarus, 251, 50–64. [10] Giuranna et al., 2021. Icarus, 353, 113406. [11] Montabone et al., 2015. Icarus, 251, 65–95. [12] Wang & Richardson, 2015. Icarus, 251, 112–127. [13] Smith et al., 2009. JGR, 114, 1–13.